International Forum on Aeroelasticity and Structural Dynamics
IFASD 2019
9-13 June 2019, Savannah, Georgia, USA

Wind Tunnel Testing of a High Aspect Ratio Wing Model

J.E. Cooper[1] R.G. Cook[1] G. Francois[1], O. de la Torre[1], S.A. Neild[1], M.H. Lowenberg[1]
S.S. Alexander[2], E.B. Coetzee[2], M. Evans[2]

[1]University of Bristol, Bristol, BS8 1TH, United Kingdom

[2]Airbus Operations Ltd., Filton, BS99 7AR, United Kingdom

Keywords: High Aspect Ratio Wings, wind tunnel testing, nonlinear aeroelasticity

Abstract: There is much current interest in the development of High Aspect Ratio Wing (HARW) designs for improved aircraft performance. However, there are a lack of relevant data sets available to validate aeroelastic modelling approaches for highly flexible wings. The design and manufacture of a highly flexible 2.4m semi-span wing is described. A series of low speed wind tunnel tests were performed to generate displacement, acceleration, strain gauge, aerodynamic pressure and six component balance measurements for a range of air-speeds and wing root angles of attack. Numerous static and dynamic measurements were made. Preliminary results are shown for the static and dynamic, structural and aerodynamic behaviour over a range of different airspeeds and wing root angles of attack.

1 INTRODUCTION

There has been much recent effort focused on reducing the fuel burn of commercial jet aircraft. High aspect ratio wing (HARW) designs are attractive as they aim to reduce the induced drag which occurs due to the presence of tip vortices. This lift induced drag can account for 40% of the aircraft's total drag in cruise [1] and is, therefore, a prime candidate for better fuel savings and aerodynamic efficiency. However, the increase in aspect ratio can have an adverse effect on the root bending moment due to the increase in moment arm of the aerodynamic loading which is likely to lead to an increase in weight. The well-known Breguet Range equation can be used to demonstrate the trade-off between reducing the induced drag balanced against the increase in weight [2].

A further complication becomes a need to suitably model HARWs which tend to be highly flexible, consequently the effects of the large deflections on the aerodynamic and structural behaviour need to be considered. Under these circumstances it is not possible to achieve accurate predictions of the static and dynamic behaviour using conventional linear modelling approaches. In particular, the nonlinear geometric effects on the aerodynamic lift, resulting shear forces and moments, flight mechanics and the 'shortening' of the wing span must be considered using non-conventional approaches.

A significant body of work has recently focused on the effects of including geometric nonlinearity into the analysis of high aspect ratio wings where a number of nonlinear beam models - a valid assumption to make on a slender structure with negligible chord-wise bending - have been developed to facilitate accurate modelling. Various approaches in the literature consider displacement-based [3, 4], strain-based [5–8], and intrinsic-based [9]

approaches to the nonlinear beam modelling problem. Generally, the aerodynamics have been modelled using lower-order models based on incompressible, inviscid and low speed assumptions. Whilst the commonly used doublet-lattice method (DLM) can be cast into the time-domain through the use of rational functions [10] or minimum-state approximations [11] in cases where nonlinearities are not due to large deformations (control surface free-play as one example), the validity of this approach is questionable in HARW applications [12]. As such, strip-theory has often been favoured for the significant computational benefits [13, 14], where a number of unsteady methods have been presented [15, 16], including models with the ability to predict viscous effects such as stall [17, 18]. However, it has been shown that 3D effects can become important [19], even for HARW applications [20], and so unsteady vortex-lattice method (UVLM) based approaches are becoming more frequently used, they can be extended to include 3D and wake effects [21, 22]. A comparison of different structural and aerodynamic modelling approaches for HARW is provided in [23].

There is currently a lack of high-quality experimental datasets available to validate geometrically nonlinear flexible wings (or indeed aeroelastic models in general). The only currently available experimental test case was performed by Tang and Dowell [24,25] and relates to a relatively small model with limited amounts of data available; however, it does provide the only widely available data relating to geometrically nonlinear static deflections and resulting Limit Cycle Oscillation (LCO) behaviour.

In this paper, some aspects of the design, construction, and testing of a 2.4m long highly flexible wind tunnel wing model are described along with preliminary experimental static and dynamic test results. Section 2 describes the philosophy behind the tests and the model design and section 3 overviews the instrumentation that was employed on the model. An overview of the tests is given in section 4 and then in section 5 a sample of the experimental results achieved for the bare beam and the full experimental set-up, both wind-off and wind-on are described. Conclusions are drawn in section 6. It is hoped that these datasets will provide further test cases to validate nonlinear aeroelastic modelling techniques.

2 HARW AWI WIND TUNNEL MODEL

As part of the UK Aerospace Technology Institute funded Agile Wing Integration (AWI) project, the design, manufacture and test of a high aspect ratio wing wind tunnel model was undertaken to:

- Validate nonlinear aeroelastic computational models of a flexible HARW
- Explore static and sub-critical dynamic aeroelastic behaviour
  - Static deflections for increasing air speed and root angle of incidence
  - Dynamic behaviour below flutter
  - Measurement of simultaneous displacement and aerodynamic data
- Explore critical dynamic aeroelastic behaviour onset and characteristics
  - Limit Cycle Oscillations due to geometric nonlinearities
  - Limit Cycle Oscillations due to stall
- Generate data sets (displacements, strains, accelerations, aerodynamic pressures) for the nonlinear HARW wing that will be made available to the aeroelastic community.

The wing was designed so that linear flutter would occur at under 70 m/s and tip deflections of around 25% semi-span could be achieved at 50 m/s with 5^{o} root angle of

attack. The ability to initiate LCOs occurring due to nonlinear geometric effects and stall driven LCOs, below the linear flutter speed, via increases in the wing root angle of attack was also a requirement. Figure 1 shows the underlying concept of the wind tunnel model with 2.4m semi-span, AR of 20 (=10 semi-span), root chord 320mm and a taper ratio of 0.5. The inclusion of taper was aimed towards ensuring that stall occurred towards the tip. A key design driver on the aerofoil thickness was to ensure that there was enough room inside the wing for all the required cabling and pressure tappings. Most of the initial design was performed using a NACA0012 aerofoil section, but this had to be increased to a NACA0015 section in the 4 sections closest to the root to enable the static pressure tappings to be carried within the wing.

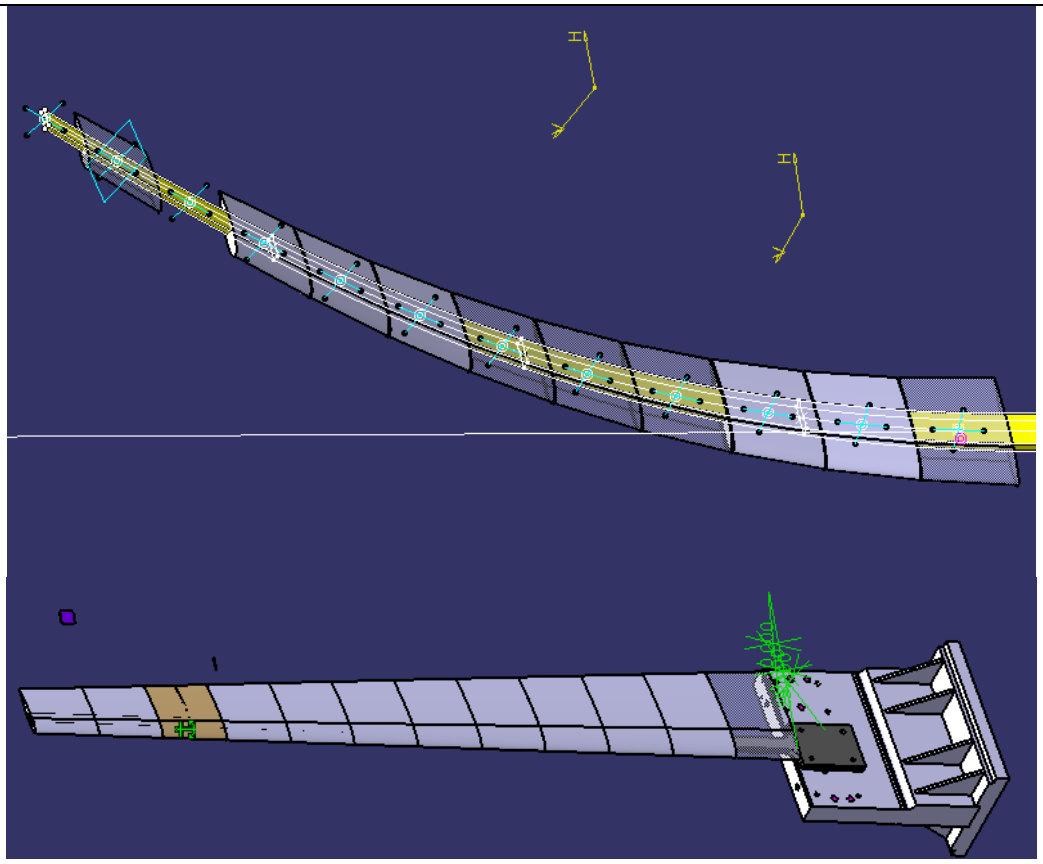

Figure 1. Initial Concept of the AWI-HARW Design

The underlying structural stiffness was derived from the beam spar manufactured from 2024 series aluminium alloy shown in figures 2 and 3. Twelve aerodynamic sections, shown in figures 4 and 5, comprised of an upper surface manufactured from a relatively stiff foam (Burnco Board 250 0.25g/cm^3 density) and an aluminium alloy lower surface. The aerofoil sections were attached to the beam via a series of lugs that can been seen in Figures 2 and 3. Such a manufacturing approach, with gaps between the sections, ensured there would be no nonlinear stiffening effect and little damping increase added to the structure following the addition of the aerodynamic surfaces. Also, the design facilitated more space within the aerodynamic sections to contain the cabling required by the various transducers. The gaps between the sections were eventually covered with tape to ensure smooth aerodynamic flows.

The final built-up wing structure, including a tip-pod, is shown in Figure 6, and the installed model in the wind tunnel is illustrated in Figure 7.

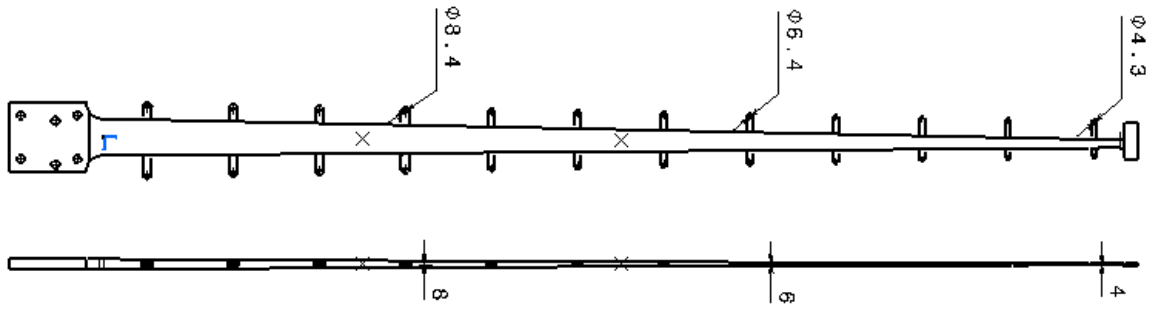

Figure 2. Spar Detail with Lugs

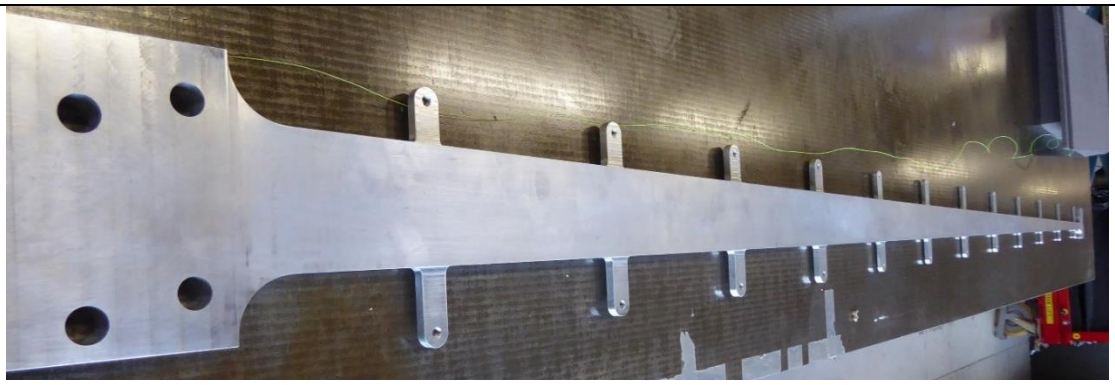

Figure 3. Wing Spar Structure - © UoB – 2019

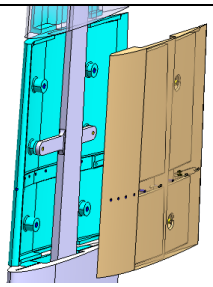

Figure 4. Schematic of Metallic (Blue) and Foam (Beige) attachment

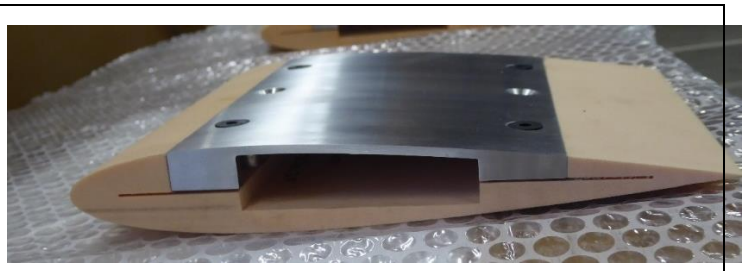

Figure 5. Metal and Foam Aerofoil Sections - © UoB – 2019

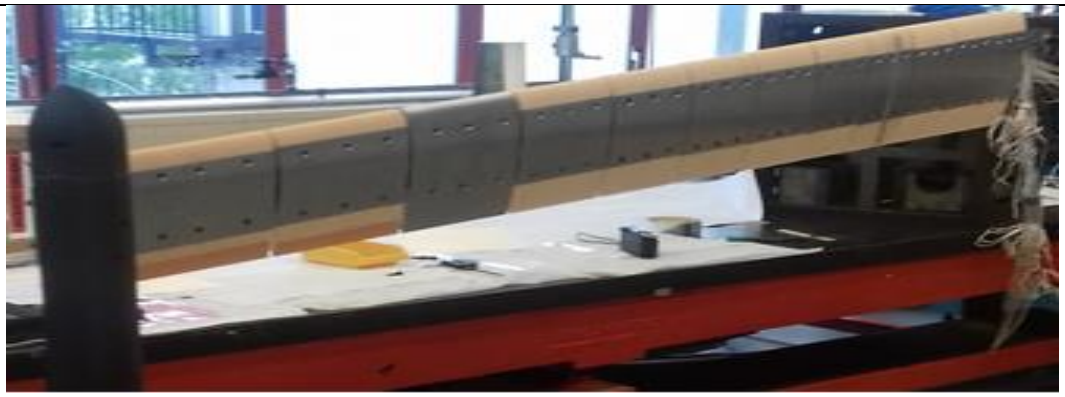

Figure 6. Built-up Wing Ready to be moved into the wind tunnel. © Airbus – 2019

Figure 7. Final Test Set-up in the Airbus Wind Tunnel - © Airbus – 2019

3 INSTRUMENTATION

A range of sensors, see Figure 8, were used during the tests to measure structural and aerodynamic data.

3.1 Structural Measurements

- 3D Cameras – 39 targets (including 3 on the tip pod) were attached to the structure and x,y,z coordinates of each point were measured simultaneously at 170Hz sampling rate.
- Strain Gauges - two pairs (upper and lower surface) of strain gauge rosettes were installed at points (1.51m and 2.05m from the beam root) on the structure that were predicted to experience the largest strains, and also a single set at the wing root. These were used for safety monitoring.
- Accelerometers – tri-axial and uni-axis accelerometers were positioned on the leading and trailing edges of several chordwise sections so in-plane, out-of-plane and torsional motions could be measured at a sampling rate of 1kHz.
- Wind Tunnel Balance – full six-component static balance readings were taken throughout the tests giving C_L, C_D, C_M, etc.

3.2 Aerodynamic Measurements

- Steady Pressure Tappings – one inboard chordwise section (#4) was instrumented with pressure tappings
- Unsteady Pressure Tappings – one outboard chordwise section (#10) was instrumented with Kulites to measure unsteady pressures
- Tunnel Measurements - a full set of wind tunnel parameters were continuously monitored during the test including: pressure, temperature, angle of incidence, dynamic pressure and Reynolds number

- Tufts – tufts were placed over the entire upper surface of the wing to enable a visual check on when and where the flow separated

3.3 Tip Pod Safety Device

The wing was manufactured with a tip-pod which contained a mass of tungsten alloy (Wolfram) that could be moved quickly using compressed-air into a different position to ensure the stability of the model as required.

3.4 Excitation

An electro-mechanical shaker, positioned below the floor of the wind tunnel as shown in figure 9, was connected to the wing via a strut which was enclosed with an aerodynamically shaped cover. The shaker was used to excite the structure with either harmonic or "chirp" inputs over frequencies from 0.1 – 18Hz.

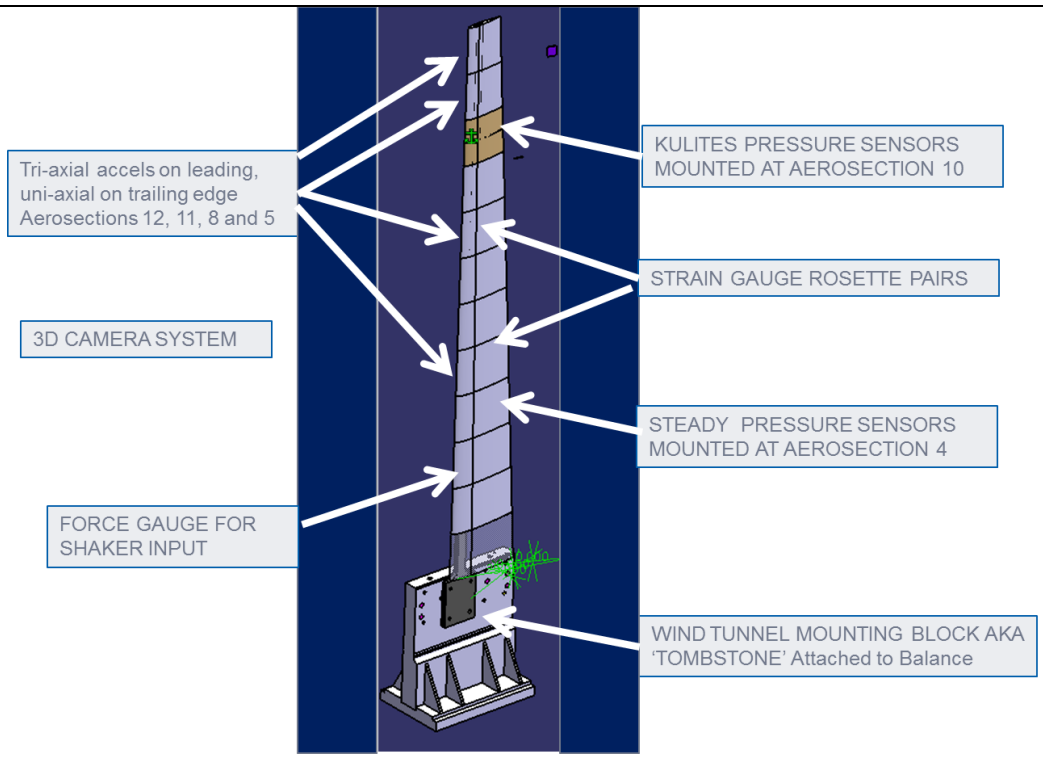

Figure 8. AWI- HARW Instrumentation

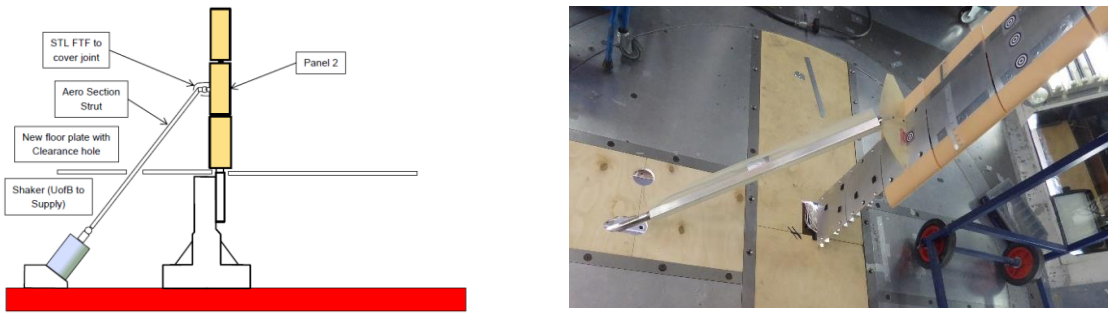

Figure 9. Schematic and photo of Shaker Set-up - © UoB – 2019

4 TESTING OVERVIEW

A range of different tests were performed on the beam structure and the fully-assembled wing to enable experimental validation of the static and dynamic characteristics both for wind-off and wind-on testing. The testing was performed at the Airbus UK Wind Tunnel Facility at Filton, Bristol. Figure 10 shows the targets that were used for the camera measurements in the wind tunnel and Figure 11 illustrates some of the aeroelastic deflections that were achieved.

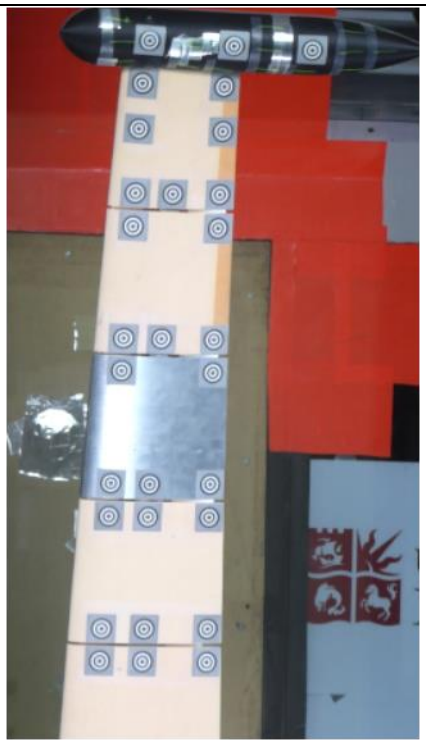

Figure 10. Camera Targets on HARW Wing
© UoB – 2019

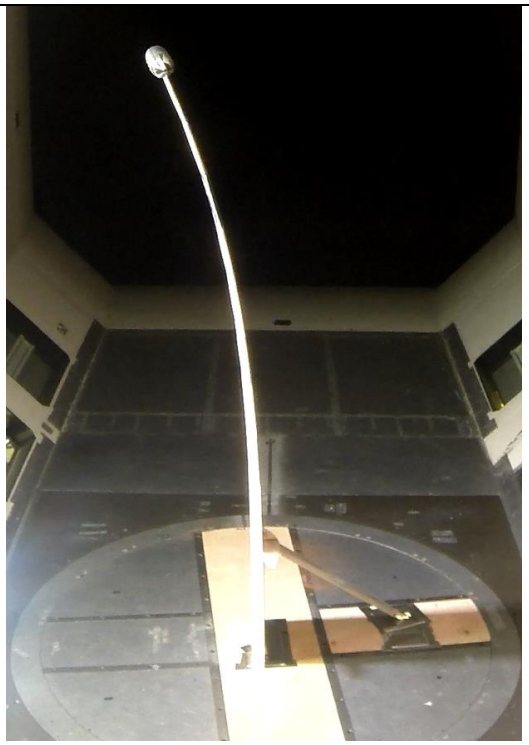

Figure 11. Example aeroelastic deflection
© Airbus – 2019

The tests included:

4.1 Beam Measurements

- Static load tests to measure the out-of-plane, in-plane and torsional stiffnesses
- Hammer (GVT) testing to measure the natural frequencies and damping ratios

4.2 Assembled Wing – Wind Off

- Hammer (GVT) testing and shaker testing to measure the natural frequencies, damping ratios and mode shapes

4.3 Assembled Wing – Wind On

- Static deflections for varying tunnel speed and angle of attack
- Hammer (GVT) testing and shaker (chirps) testing to estimate the natural frequencies and damping ratios at different airspeeds
- Measurement of the aerodynamic coefficients for increasing angle of attack
- Harmonic excitation using the shaker to measure the unsteady aerodynamic pressures for simultaneous heave and pitch motions

Tables 1 and 2 describe the types of test that were performed, 850 tests during the 206 runs that made up the wind tunnel campaign. Five different configurations were considered with different amounts of tape applied between the aerofoil sections ("partially taped" means fully taped on the compressive side and segments 1 – 7 on the tension side), with and without the shaker, and also with and without the tip-pod and safety device attached.

There were different types of test undertaken for each of these configurations to investigate different parts of the aeroelastic modelling process:

- Alpha-polar tests - slowly increasing the wing root AOA in quarter degree increments
- Chirps - fast sine-sweeps (both increasing and decreasing frequency) using the shaker
- Harmonics – shaker excitation at the resonant frequencies at different tunnel conditions
- LCO investigation – tests that resulted in Limit Cycle behavior from a range of different excitation signals
- Push release – the model was pushed into a deflected configuration using a rod from outside of the tunnel and then suddenly released.

The results described in this work relate to the clean wing configuration.

Table 1. Wing Configurations Considered

Run Types	**Events (Number %)**	**Runs (Number %)**
Tip pod + shaker but no tape	662 (78%)	140 (68%)
Partially taped wing + tip pod + shaker	58 (7%)	25 (12%)
Tip pod and partially taped wing	42 (5%)	12 (6%)
Tip pod + shaker + fully taped	67 (8%)	12 (6%)
Clean wing (fully taped)	21 (2%)	17 (8%)

Table 2. Wind Tunnel Run Types

Run Types	**Events (Number %)**	**Runs (Number %)**
Alpha Polar	50 (6%)	38 (19%)
Chirp Up / Down	314 (37%)	91(45%)
Harmonics	301 (36%)	31 (15%)
LCO Investigation	165 (20%)	38(19%)
Push – Release	10 (1%)	6 (3%)

5 PRELIMINARY RESULTS

The initial tests that were performed involved testing of the underlying beam structure so that the FE model could be updated before moving onto the built up-structure, followed by the wind-on tests. The beam was rigidly attached at its root to a solid block so as to behave as a cantilever. Both static and dynamic tests were undertaken.

5.1 Beam Measurements

5.1.1 Static Testing - Deflections

It was possible to set up the experimental configuration so that loads applied to the beam induced either out-of-plane or in-plane bending, depending upon the beam's orientation. A weight hanger was used to apply the loads at the end of the beam; the loads could either be applied at the centre of the cross-section so that only bending deflections occur, or at the end of the weight hanger so that a combined bending / torsion load was applied. Figure 12 shows

the different loading configurations. The loading sequence was applied several times to ensure the repeatability of the results. Deflections were measured using the 3D camera system with targets attached to the beam to enable motions in all three coordinates to be detected.

Figures 13 and 14 show the deflections along the beam in all 3 coordinates for in-plane and out-of-plane tip loading cases. It can be seen that there is a good repeatability between the results and that the nonlinear model gives a much better prediction compared to the linear model. There is a small amount of coupling between in-plane and out-of-plane motions which is not predicted by the models, most probably due to imperfections in the symmetry of the loading conditions. Tables 3,4 and 5 confirm the accuracy of the numerical models, particular once an addition of 2% to the out-of-plane stiffness and a reduction of 5% in the torsional stiffness was made to the beam models.

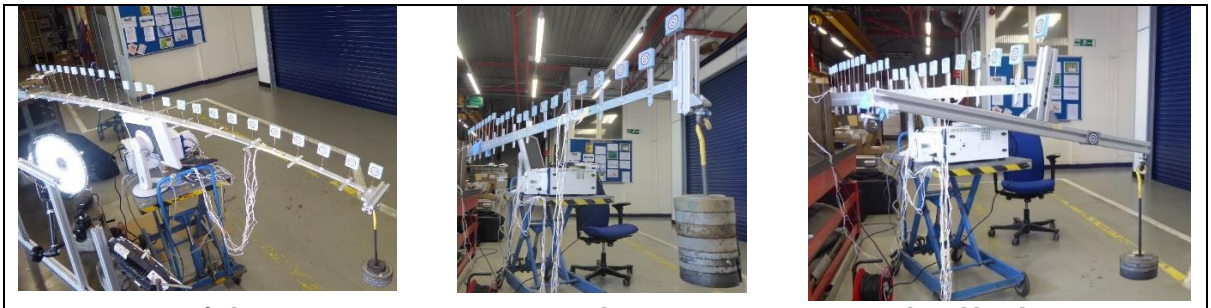

Out-of-plane In-plane Combined bending-torsion

Figure 12. Static Loading Testing of Bare Beam © UoB – 2019

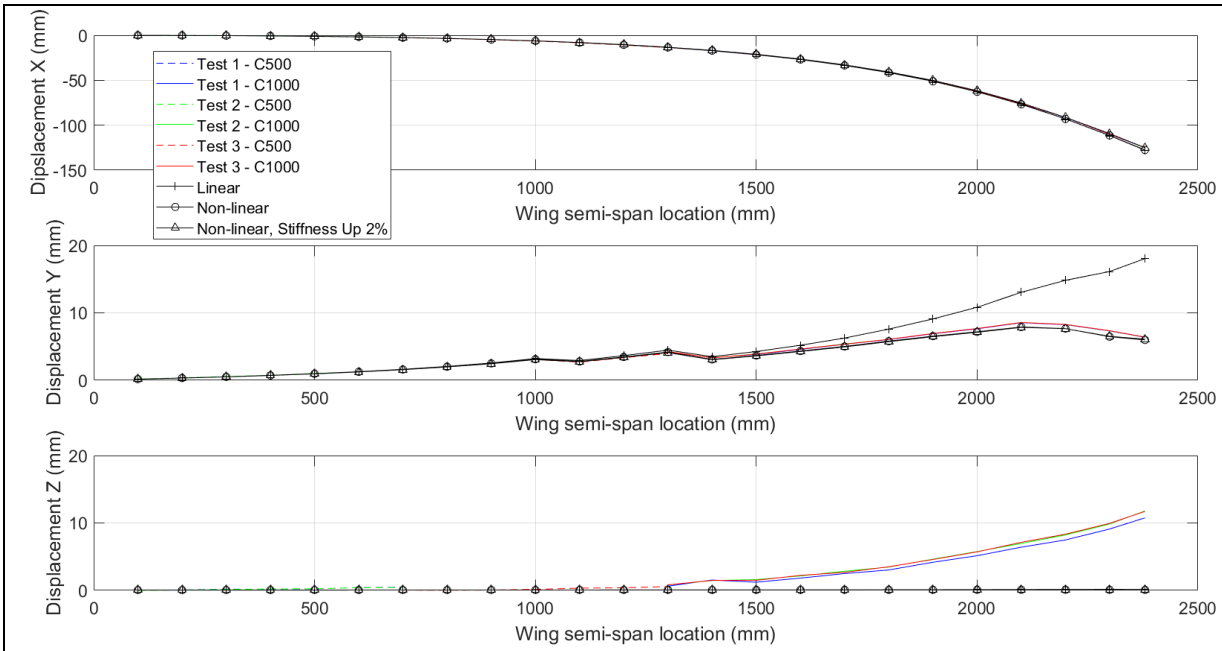

Figure 13. Displacements (x out-of-plane, y spanwise, z in-plane) along the beam for out-of plane loading of 1.944Kg

Table 3. Tip Out-of-Plane Deflections. Out-of-Plane loading case

	1.723 kg		**1.944 kg**	
	mm	% difference	mm	% difference
Experiment	**111.7**		**124.9**	
Linear FE	113.3	1.4	127.8	2.4
Nonlinear FE	113.2	1.3	127.5	2.1
NL Beam code	110.9	-0.7	124.6	-0.2
Linear FE (102%)	111.1	-0.5	125.4	0.4
NL FE (102%)	111.1	-0.5	125.1	0.2
NL Beam code (102%)	108.8	-2.6	122.3	-2.1

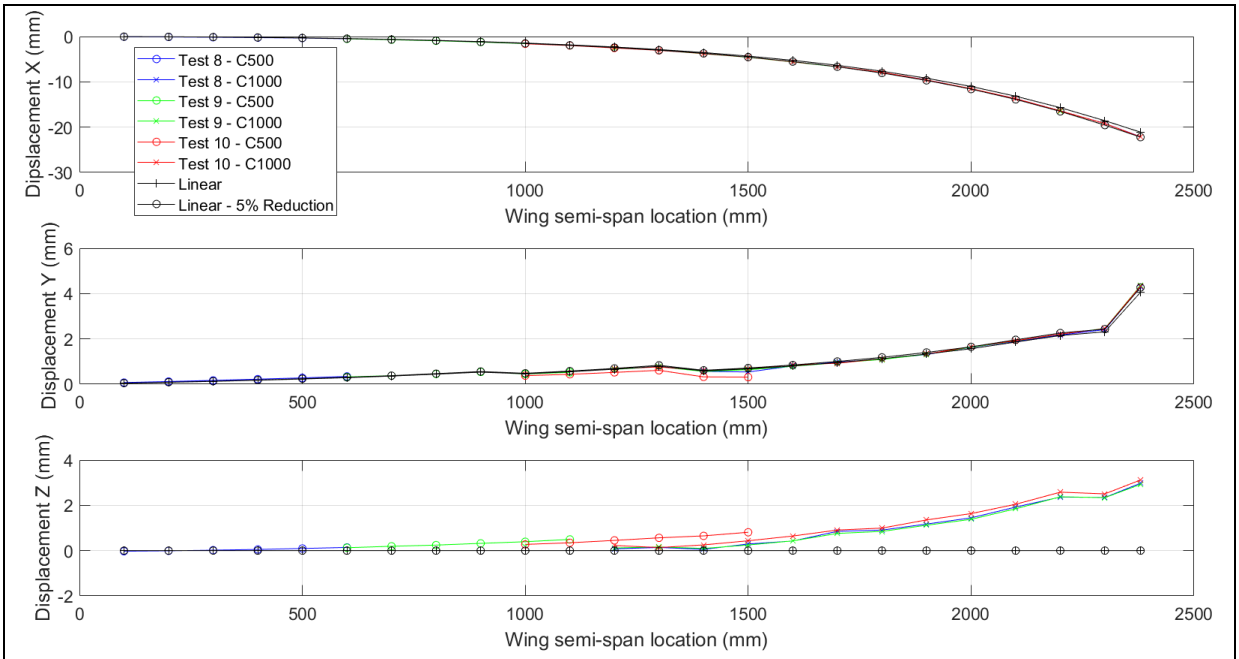

Figure 14. Beam deflections (x in-plane, y spanwise, z out-of-plane) for 6.723Kg in-plane loading

Table 4. Tip Out-of-Plane Deflections. In-Plane loading case

	2.723kg		6.723kg	
	mm	% difference	mm	% difference
Experiment	**8.95**		**22.15**	
Linear FE	8.55	-4.53	21.10	-4.72
Nonlinear FE	8.55	-4.5	21.09	-4.8
NL Beam code	8.56	-4.36	21.14	-4.56
Linear FE (95%)	9.00	0.5	22.22	0.3
NL FE (95%)	9.00	0.5	22.21	0.3
NL Beam code (95%)	9.01	0.7	22.25	0.5

Table 5. Out-of Plane deflections for torsion tests.

	1.723kg				2.223kg			
	Tension		Comp		Tension		Comp	
Experiment	**17.31**	% diff	**-17.40**	% diff	**26.03**	% diff	**-25.44**	% diff
Linear FE	17.02	-1.68	-17.02	-2.18	21.90	-15.87	-21.95	-13.71
Nonlinear FE	19.46	12.4	-19.46	12.7	25.67	-1.4	-25.94	2.0
Beam model	19.44	12.32	-19.74	13.45	25.67	-1.39	-26.08	2.52
Linear FE updated	17.02	-1.7	-17.02	-2.2	21.96	-15.6	-21.96	-13.7
Nonlinear FE updated	19.38	12.0	-19.54	12.3	25.56	-1.8	-25.82	1.5
Beam model updated	19.37	11.9	-19.66	13.0	25.55	-1.8	-25.96	2.1

5.1.2 Static Testing - Strains

Strain gauge readings were taken simultaneously at the same time as the deflection measurements. Figure 15 shows the largest measured principal strains for the root and middle tension / compression rosettes for the out-of -plane loading case. There is a clear linear variation of the strain vs. weight for all three rosettes. The strain is much greater at the middle set of rosettes and there is a good symmetry between readings on the top and bottom surfaces. Table 6. shows an example of the good comparison achieved between the experimental strain measurements and the intrinsic beam modelling predictions for the middle strain gauge rosette tension side. Tables 6 and 7 show very small principal angles, indicating that there is very little bending-torsion coupling; these small values amplify the differences between the small modelled predictions and experiments. A similar good comparison between modelling and test strains was found for the other two load cases (in-plane and torsion).

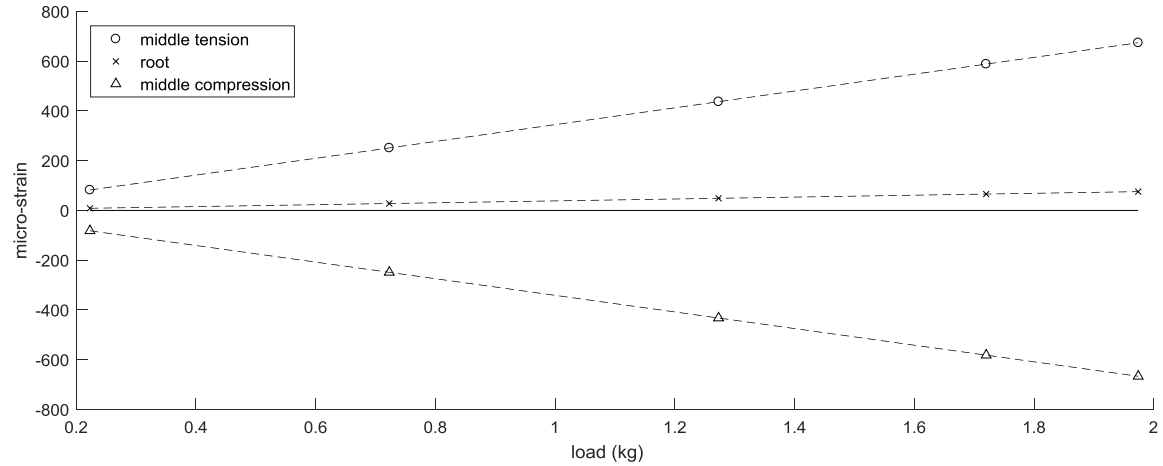

Figure 15. Principal strain values at three rosettes for out-of-plane loading.

Table 6. Averaged Delta Principal Strains and Angles for Middle Strain Rosette – Tension Side

(Load Kg)	$\delta\,\varepsilon_{p1}$ Exp	$\delta\,\varepsilon_{p1}$ Model	$\delta\,\varepsilon_{p2}$ Exp	$\delta\,\varepsilon_{p2}$ Model	θ_p (deg) Exp	θ_p (deg) Model
0.223	78.72	80.90	-24.87	-26.70	-0.63	-0.05
0.723	251.27	261.00	-79.51	-86.14	-0.71	-0.08
1.223	419.85	438.46	-132.95	-144.70	-0.56	-0.08
1.723	583.43	612.29	-184.76	-202.06	-0.72	-0.09
1.974	652.00	687.74	-206.39	-226.96	-0.71	-0.09

Table 7. Experimentally Measured Principal Angles for Different Load Conditions

(Load Kg)	θ_p (deg) Root	θ_p (deg) Middle tension	θ_p (deg) Middle compression
0.223	1.19	-2.45	-0.63
0.723	0.46	-2.36	-0.71
1.223	0.51	-2.45	-0.56
1.723	0.38	-2.31	-0.72
1.974	0.57	-2.30	-0.71

5.1.3 Dynamic Testing

A vibration test was performed to measure the natural frequencies, damping ratios and mode shapes of the bare beam structure. These results were used to validate the dynamic FE model and also to determine the level of damping in each mode. Two types of input were used: impact testing (in-plane and out-of plane) using an instrumented modal hammer and also a push-release excitation. Four averages were taken for each test cases. Responses to the

excitation were recorded using the embedded accelerometers and also a subset of the 3D camera targets, both measuring the outer half of the wing. An initial data analysis was performed using a simple peak peaking / log decrement approach, followed by a more detailed investigation analysis using the ERA (Eigensystem Realisation Algorithm) method [26].

Figure 16 shows a typical measured Frequency Response Function and corresponding curve-fit, with Table 8 listing the identified natural frequencies and damping ratios, and Figure 17 showing the first four experimental mode shapes. Note that the cameras only measured the outer half of the wing. The modal behaviour is as expected with a series of out-of-plane and in-plane bending modes; note the spatial aliasing in the mode shape plots due to the sparse distribution of measurement points. There are many bending modes before the first torsion mode occurs due to the high aspect ratio and severe taper ratio.

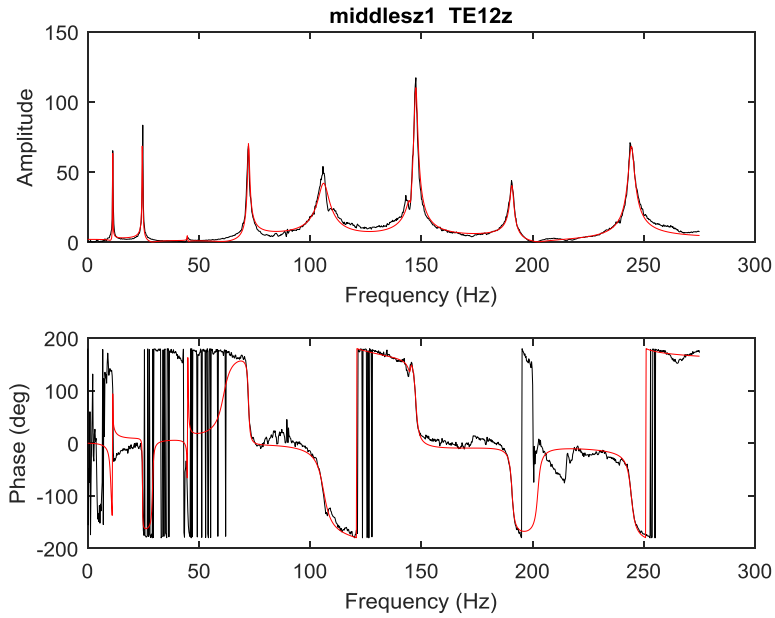

Figure 16. Sample Out of Plane FRF and Curve-fit from Impact Excitation

Table 8. Identified Bare Beam Modal Parameters

Freq (Hz)	Damping (%)	Type	Freq (Hz)	Damping (%)	Type
4.28	0.36	Bending	72.29	0.64	Bending
11.23	0.26	Bending	106.07	2.39	Bending
17.86	0.62	Fore/aft	112.93	1.90	Fore/aft
24.59	0.33	Bending	145.04	0.46	Bending
44.82	0.19	Bending	148.53	1.53	Torsion
49.61	2.09	Fore/aft			

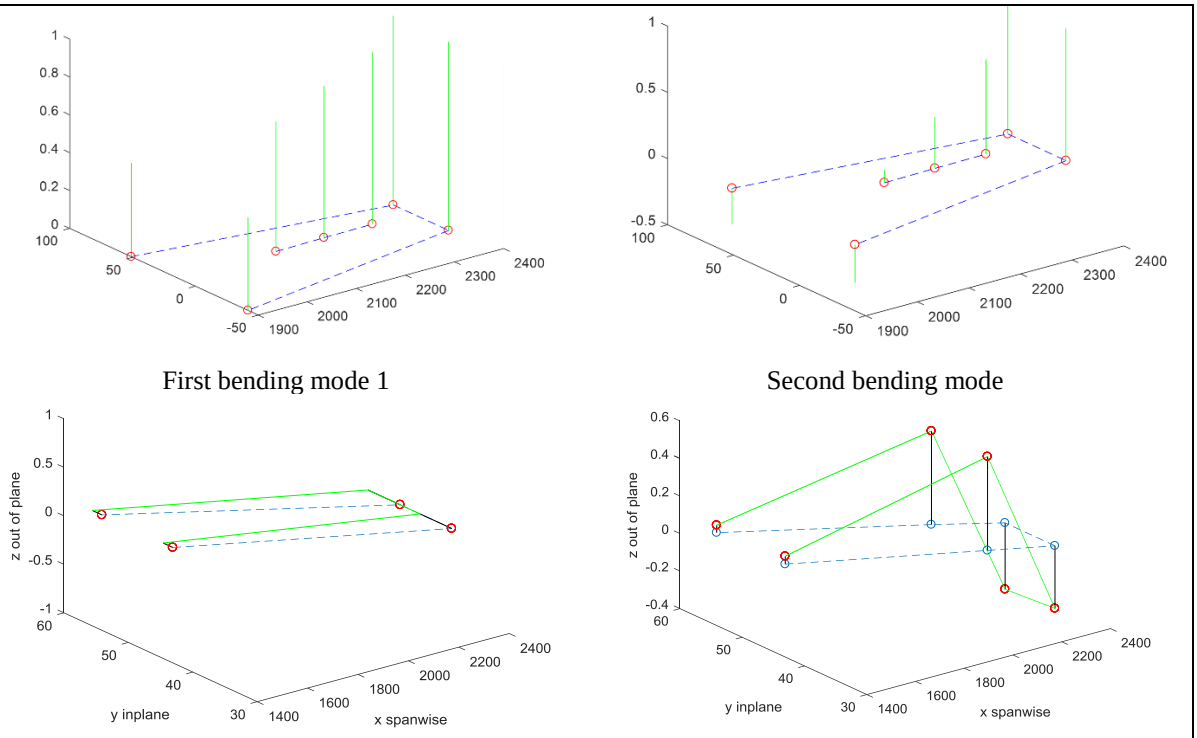

First bending mode 1 Second bending mode

First fore-aft mode Third bending mode

Figure 17. Experimentally Measured Bare Beam Mode Shapes

5.2 FULL BUILD TESTING

Following the testing of the bare beam structure, the wing was instrumented and then the aerodynamic panels attached, as shown in Figure 7. The results shown in this section relate to the clean wing configuration.

5.2.1 Wind–off Dynamic Testing

Before the wind tunnel tests started, vibration tests were performed on the full wing structure in order to determine how much the natural frequencies changed due to the inertia of the aerodynamic panels, cabling / tubing and tip-pod. A further consideration was the damping added by the built-up structure. Excitation was provided using the modal hammer, push-release and also the underfloor shaker. Modal parameter estimation was performed once again using the ERA method.

Figure 18 and Table 9 show the modal parameter estimates for the first four modes that were determined from the modal hammer tests. Compared to the bare beam tests it can be seen that the natural frequencies have reduced due to the added inertia of the aerodynamic sections and the cabling / tubing. Although the damping ratios have roughly doubled in magnitude, they are still relatively low primarily due to having separate aerodynamic sections.

Table 9. Identified Full Build Modal Parameters

Freq (Hz)	Damping (%)	Type
2.25	0.760	Out of plane bending
7.27	0.818	Out of plane bending
10.30	1.119	Fore-aft bending
15.03	0.609	Out of plane bending

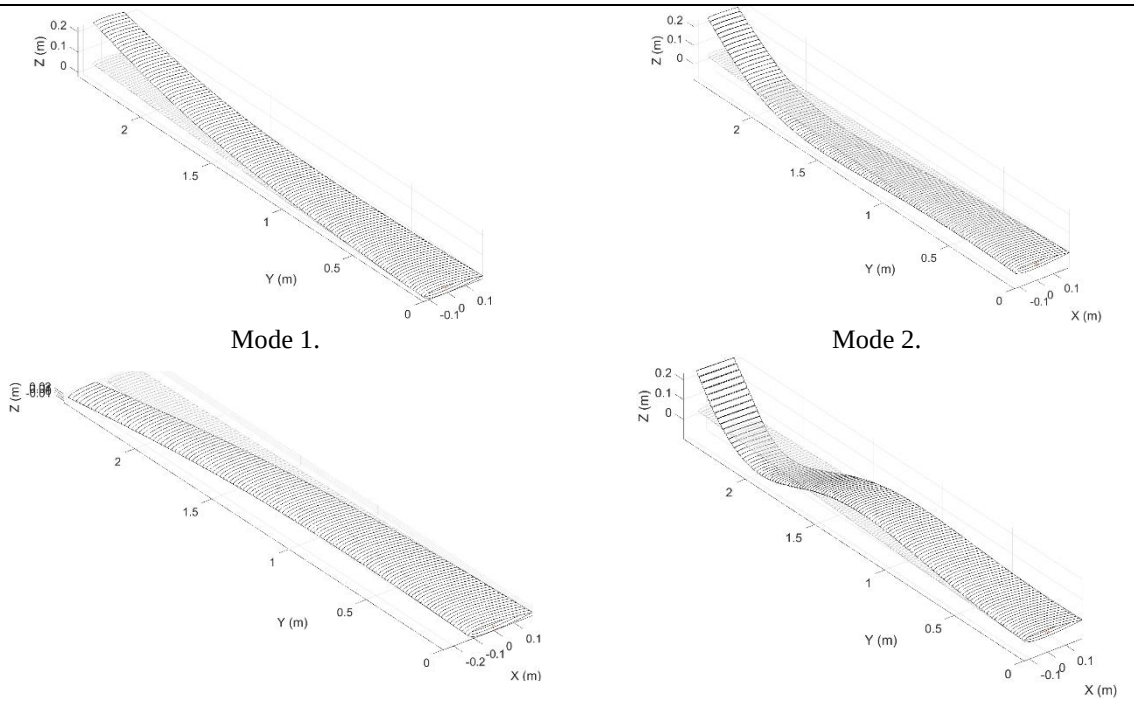

Mode 1. Mode 2.

Mode 3. Mode 4.

Figure 18. Identified mode shapes – clean wing configuration

5.2.2 Wind-on Testing – Chirp and Transient Excitation

Excitation to the wing was provided using a chirp excitation via the shaker or push-release. The measured responses were used to compute FRFs from which the wing natural frequencies and damping ratios for different airspeeds and root AoA can be computed. Figure 19 shows a typical chirp excitation signal and the corresponding accelerations in 3 directions, and figure 20 shows the related power spectra. Finally, figure 21 shows frequency and damping trends versus airspeed; as flutter is predicted to occur at over 100m/s for the no tip-pod condition flutter, no instabilities occurred in the speed ranges that were considered. There is very little damping on the in-plane mode as this has little interaction with the aerodynamic forces.

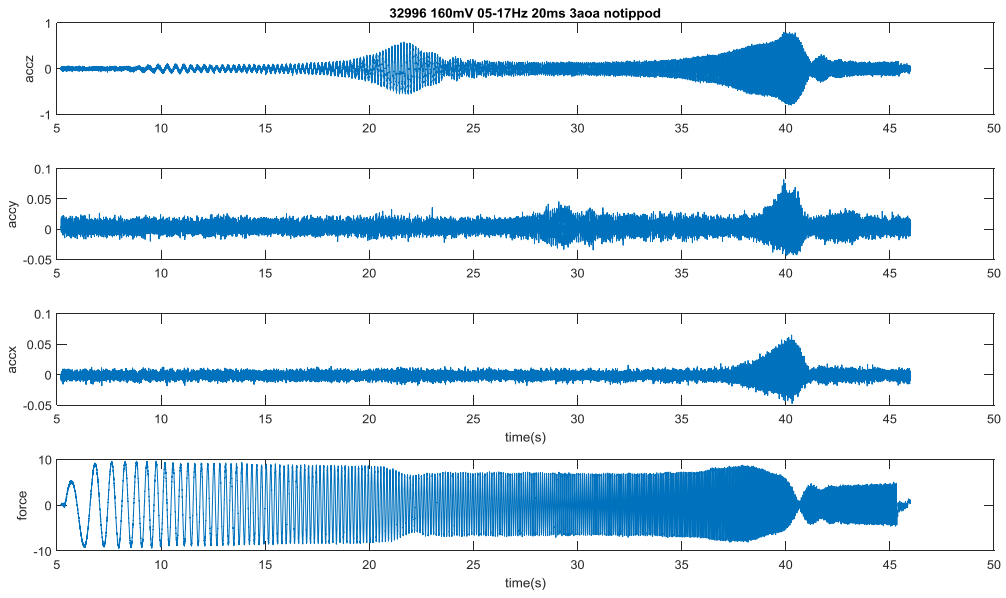

Figure 19. Chirp input and resulting acceleration responses at 20 m/s and 3º root AOA

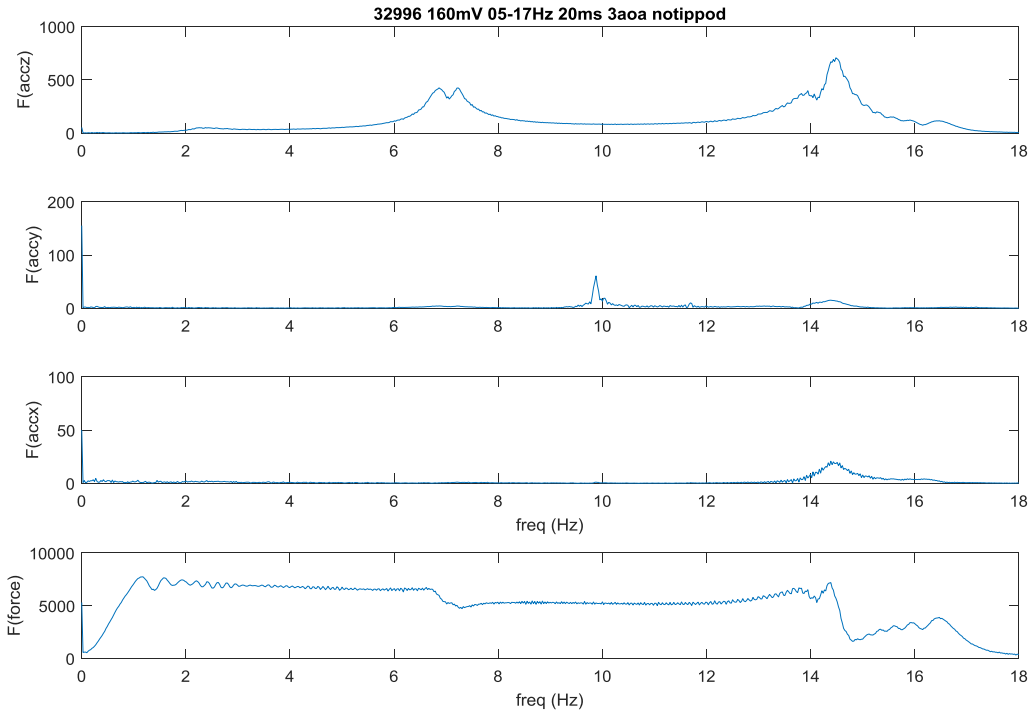

Figure 20. Typical power spectra for chirp excitation and corresponding acceleration responses.

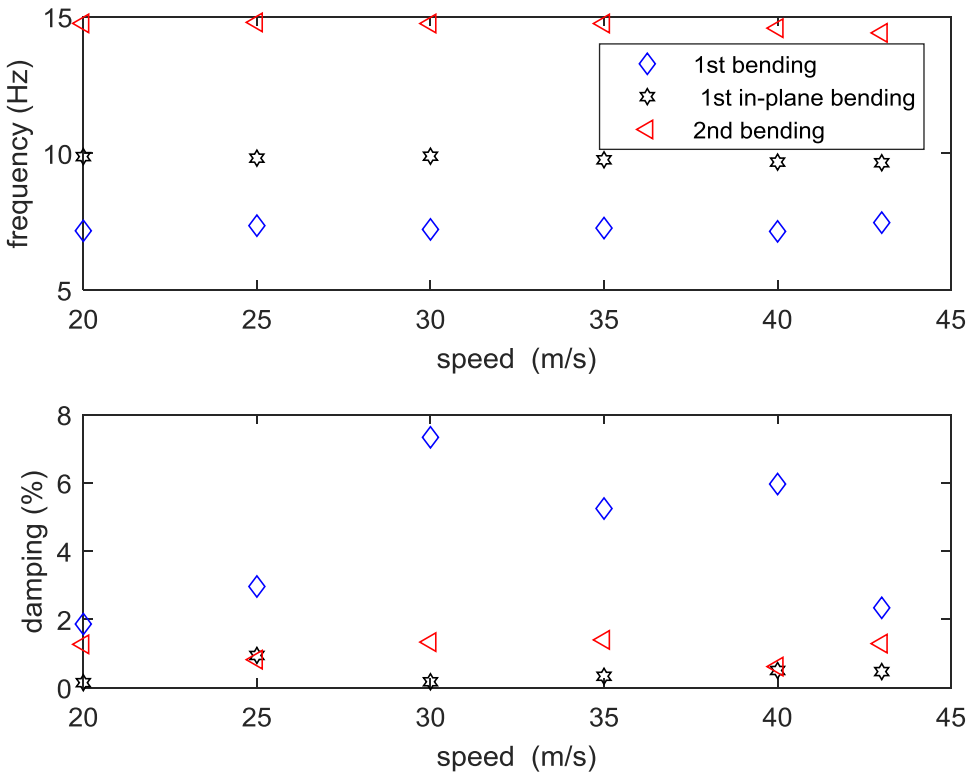

Figure 21. Frequency and damping trends vs airspeed

5.2.3 Wind-on Testing – Harmonic Excitation

Having determined the natural frequencies at each tunnel condition (speed and root AOA), harmonic excitation was applied at each natural frequency and the resulting responses and unsteady aerodynamic pressures measured. The objective of these tests is to examine the unsteady aerodynamic behaviour for the heave and pitch motion at section 10 which contained the Kulites, investigating any attenuation and phase lag for increasing reduced frequency, and also detecting any possible nonlinearities that might occur in the unsteady aerodynamic pressures. It can be seen in figure 22 that there is a direct correlation between the force and the resulting structural motion, however, the unsteady aerodynamic pressure is not a pure sinusoid, containing possible harmonic terms which require further investigation.

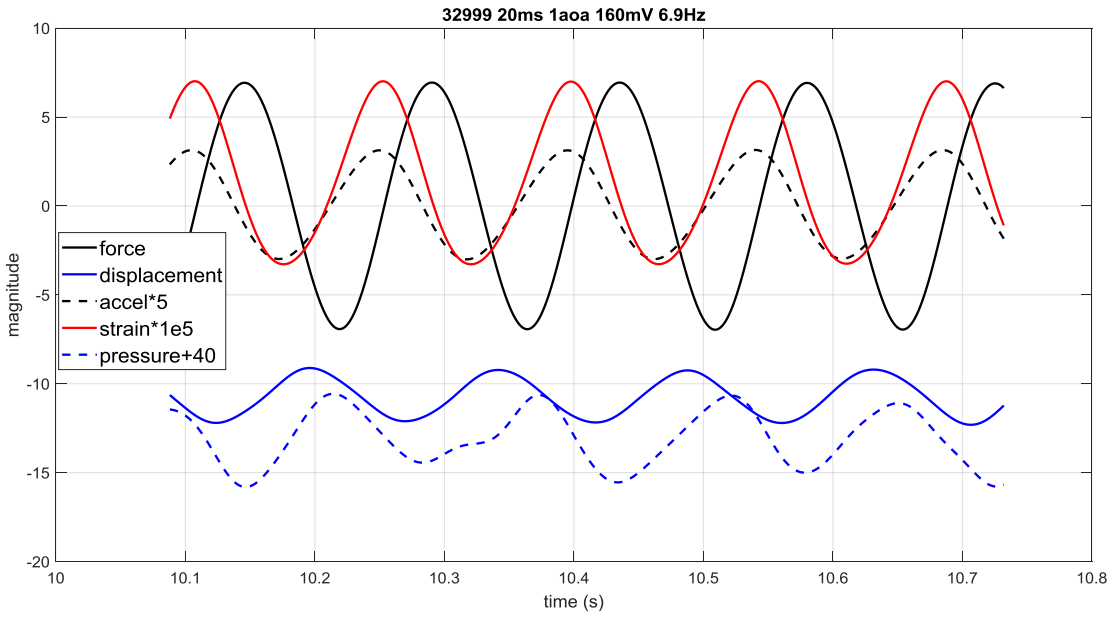

Figure 22. Unsteady aerodynamic pressures, strain and accelerometer vs time

5.2.4 Wind-on Testing – Static Aeroelastic Behaviour

The static aeroelastic characteristics of the HARW model were explored by varying the root AOA by ¼ degree increments at different tunnel speeds (20m/s, 25m/s, … ,50 m/s). Deflections were measured using the 3D camera system, aerodynamic pressures determined at two chordwise strips (sections 4 and 10) using the pressure tappings and the Kulites respectively, and wind tunnel balance readings taken at all conditions.

Figure 23 shows the wing-tip deflection in out-of-plane (z), in-plane (y) and spanwise (x) for varying root AOA at different speeds. Each test condition was held steady for 10 seconds and the mean and variance of the deflections computed. It can be seen there was a significant variation in the deflections at the largest AOAs due to a considerable amount of flow separation that occurred in these conditions. Although the greatest deflection is in the out-of plane direction, there is also a large amount of spanwise deflection, due to the nonlinear geometric effects resulting from the flexibility of the wing, and also a considerable amount of in-plane deflection due to drag and coupling effects. The rate of increase of the out-of-plane deflection reduces as the total deflection grows.

The nonlinear geometric behaviour is illustrated further in Figure 24 where the out-of plane deflections are shown along the span of the wing for different AOAs and airspeeds. The

geometric shortening effect is clearly visible and also the reduction in the increase of out-of-plane deflection with growing AOA. For the 20 m/s case, it can be seen that the loss of lift associated with the separated flows at larger AOAs results in less deflection for the 14 degree AOA case compared to those for the 10 and 12 degree cases.

Figure 25 shows the centre of pressure determined from the measured aerodynamic pressures at sections 4 (pressure taps) and 10 (Kulites) for varying AOA at three different airspeeds (20, 35, 50 m/s). It can be seen that beyond small AOAs the centre of pressure remains close to the quarter chord position, although it does start to move aft a little for the Kulite section at the highest speed case.

The measured wind tunnel balance coefficients for the three speed cases are shown in figure 26. For the 20m/s condition, the lift-curve slope is linear (at around 0.08/deg) but starts to tail off around 10^o. When most of the flow separates across the wing the value of C_L levels off at about 13^o. The drag coefficient increases in a roughly exponential manner with increasing root AOA up to 13^o when it then increases dramatically, which again corresponds with most of the flow separating. The side force increases with AOA up to around 13^o which is expected as the bending deflection of the wing increases the spanwise component of the lift. For large out-of-plane and in-plane bending deflections the effective AOA is not simply the sum of the root and elastic rotations, and this effect is seen with the pitching moment coefficient which reaches a maximum value around 5^o and then reduces before plummeting once the stall condition is reached.

Similar behaviour is found for the 35m/s and 50 m/s cases. The linearity of the lift-curve slope stops at a lower AOA and the pitching moment now becomes negative, a function of the coupled bending and torsion deflections.

Local pressure coefficients were calculated across chordwise sections 4 and 10 using the pressure tappings and Kulites, respectively, for the same speed cases as above, and these can be seen in Figure 27. For the 20m/s case there is a very good agreement on both segments for the lift and moment coefficients up to around 7deg when the inboard values are greater than the outboard values, presumably due to flow separation effects. Beyond 10 deg there lift/curve slope levels off. Note that the moment coefficients have been plotted as nose down positive. There is a significant difference between the drag coefficient values with the inboard values showing a linear trend whereas the outboard values remain more or less constant until 11 deg when there is a dramatic increase in the drag. The trends at 35 m/s are similar for all coefficients. For the 50m/s case there is a much greater difference between the inner and outer section coefficients due the greater out-of-plane and in-plane bending deflections and the increase of separated flow along the span.

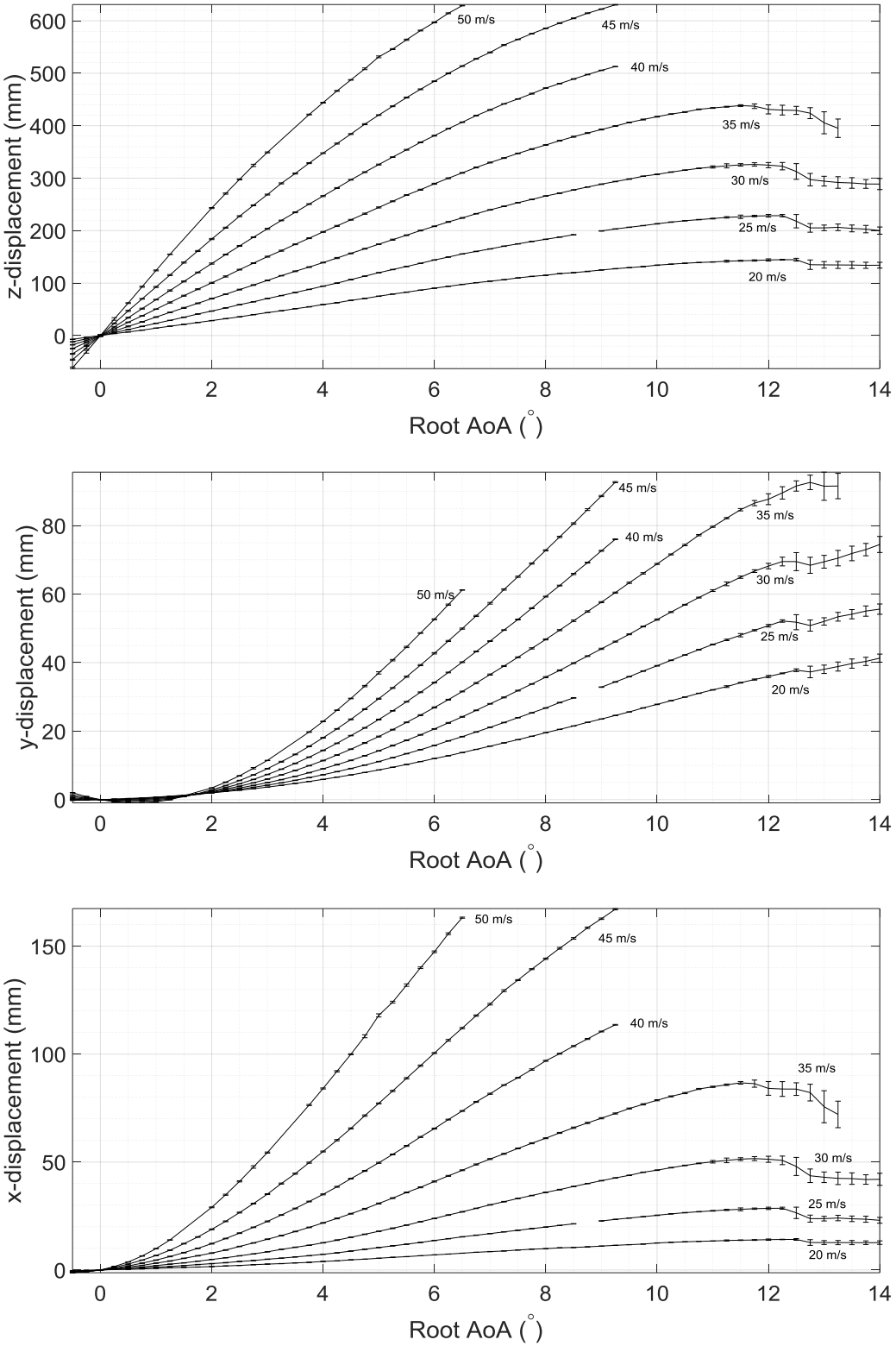

Figure 23. Tip Displacements for z (out-of-plane), y (spanwise) and x (in-plane) coordinates for 20, 25, ..50 m/s

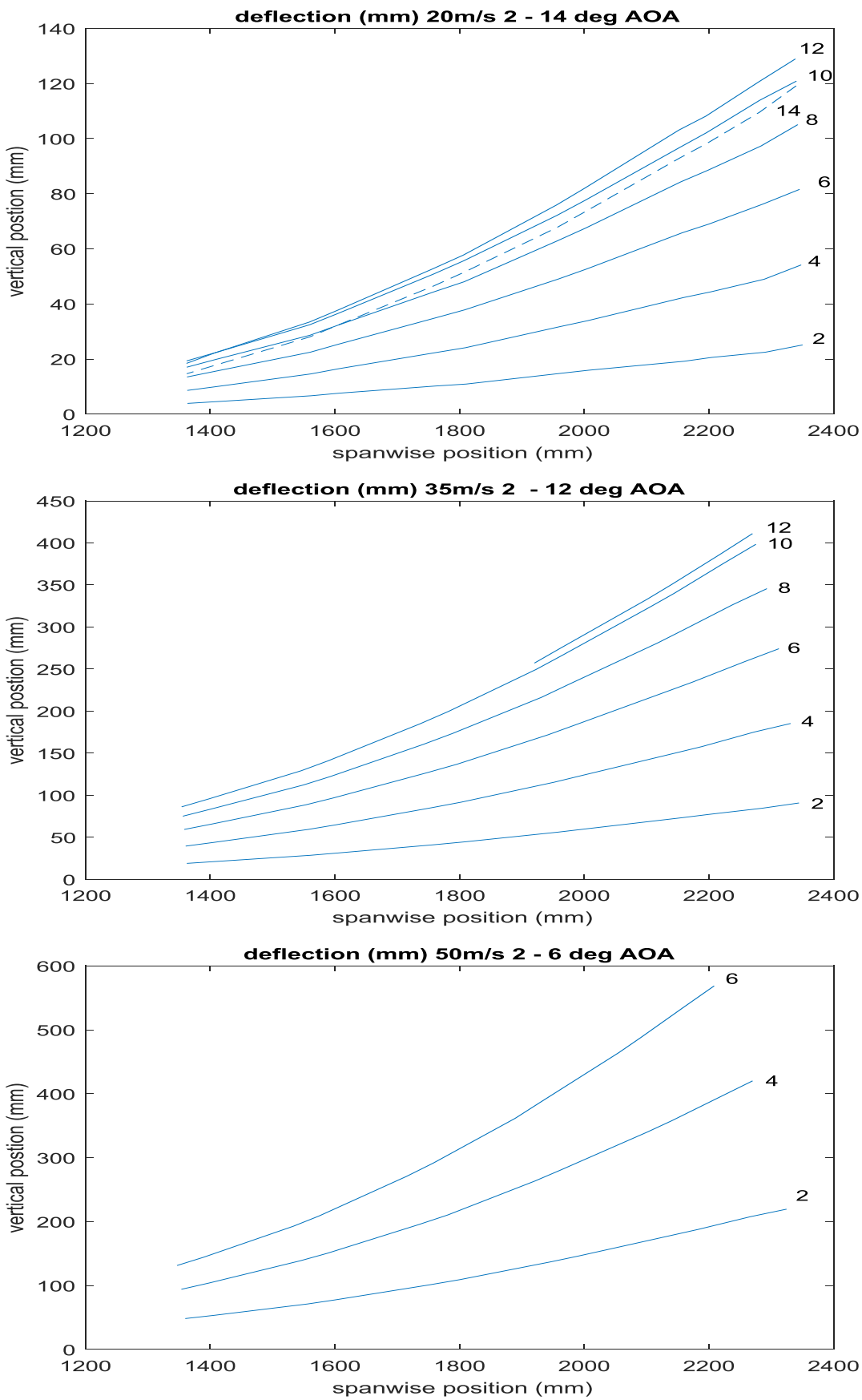

Figure 24. Vertical deflection vs spanwise position along the HARW model at 20m/s, 35m/s and 50m/s for different AoAs

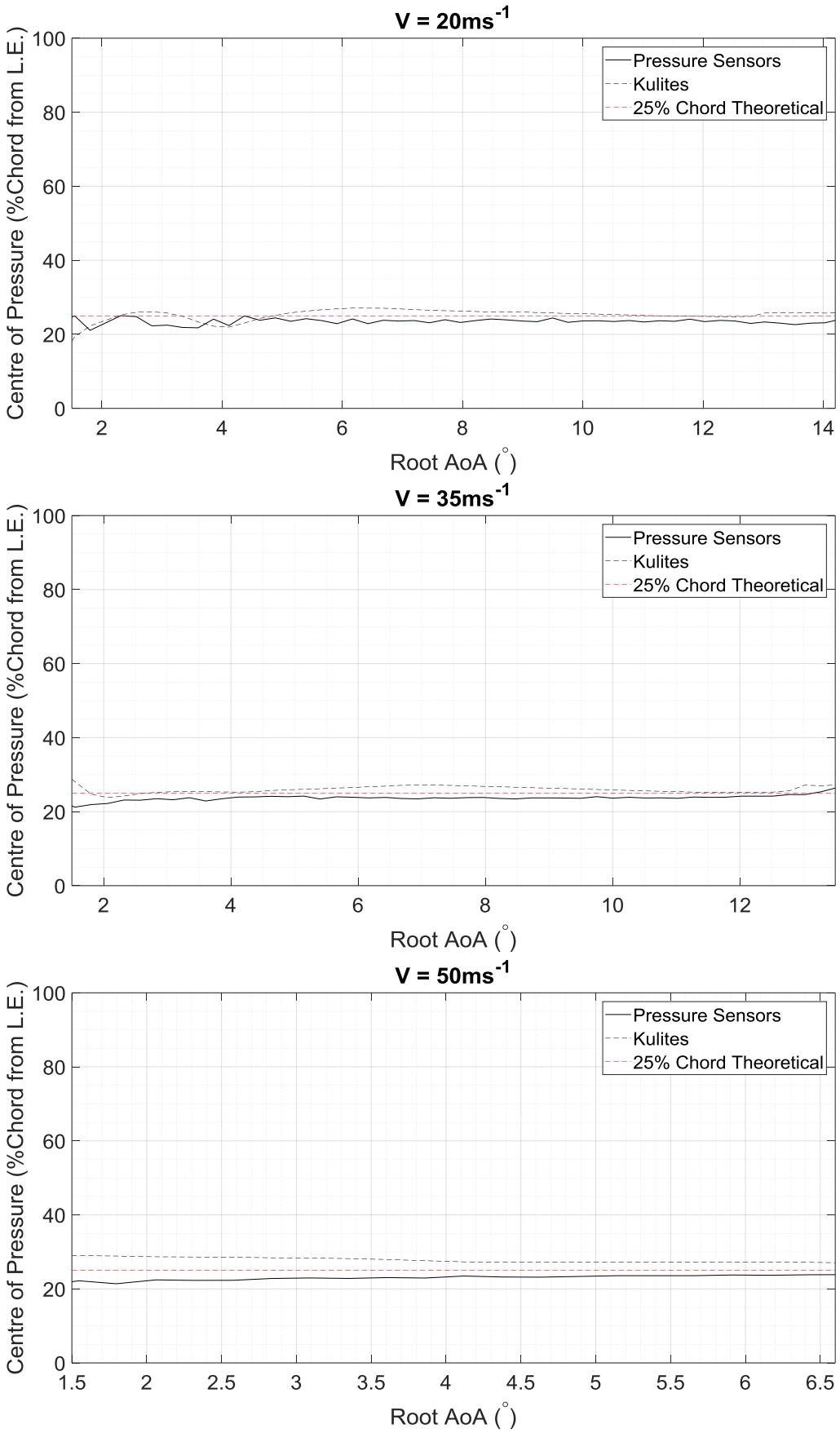

Figure 25. Centre of pressure from pressure tapping and Kulite sensors vs root AOA at 20m/s, 35m/s and 50 m/s

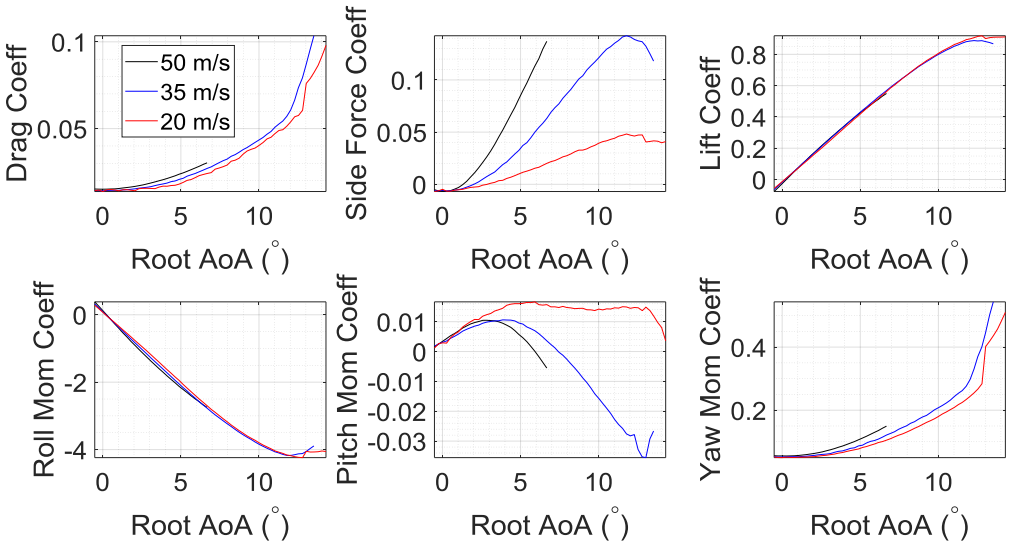

Figure 26. Wind Tunnel Balance Coefficients for varying Root AOA 20m/s, 35 m/s, 50m/s

5.2.4 Wind-on Testing – Limit Cycle Oscillations

The final part of the test campaign concerned the occurence of Limit Cycle Oscillations (LCOs) and their characteristics. Two types of LCOs were sought, those resulting from stall, and others resulting from the nonlinear geometric behaviour. Figure 28 shows an example of an LCO that occurred at 20 m/s following an increase in the root AOA to a critical value. The upper time history shows the out-of-plane deflection for the LE at an outboard part of the wing (z3) and it can be seen how the deflection increases with AOA until an LCO occurs. The other two plots show a magnified section of the LCO behaviour for the LE and TE on the same chordwise cross-section. It is apparent the LE(z3) and TE (z4) response are in-phase, indicating that the motion is primarily a bending motion with little torsion.

Figure 29 shows the resulting deflections of this strip for all three coordinates and the LCO motion can be seen to involve a coupled in-plane / out-of-plane motion. Figure 30 shows the averaged spectra of the LCO motion which consists primarily of a response at 2.38Hz but with some harmonic content at around 6.88Hz and other frequencies.

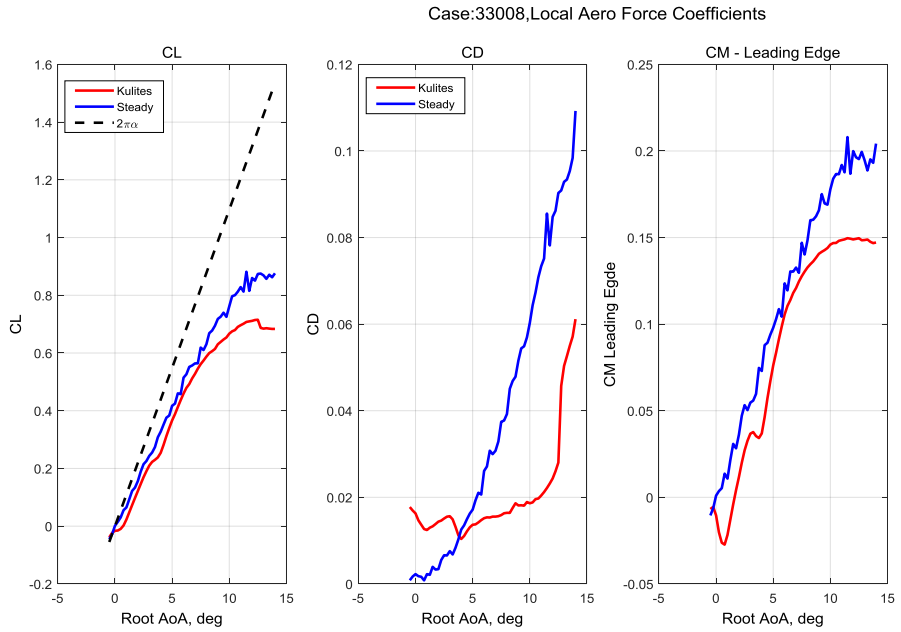

20 m/s

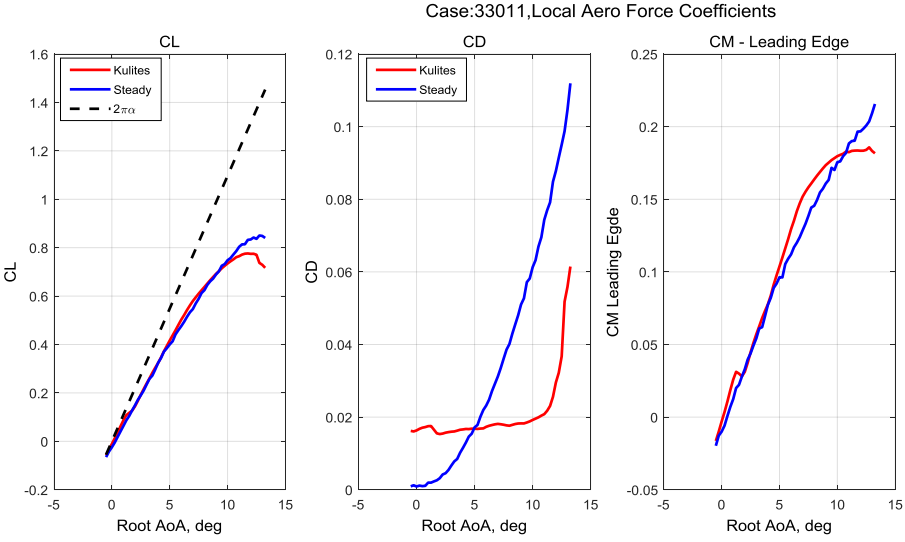

35 m/s

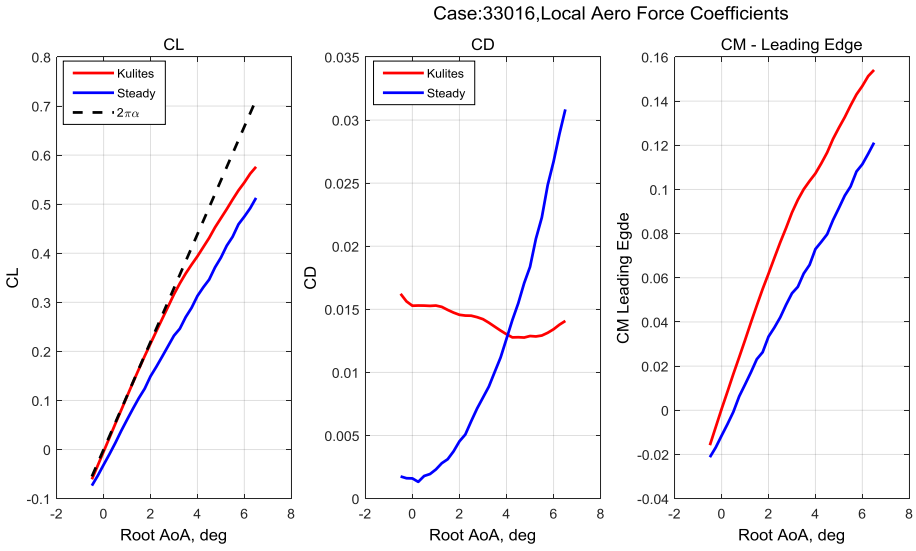

50 m/s

Figure 27. Force Moment Coefficients from Pressure Tappings and Kulites 20m/s, 35m/s, 50m/s

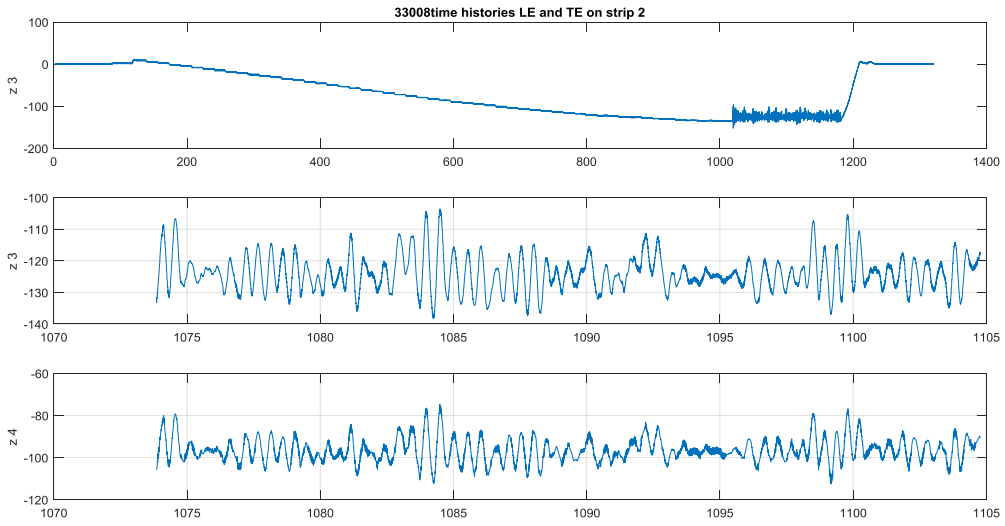

Figure 28. Out of plane deflections for increasing root AOA up to LCO and detail of LCO for LE (z3) and TE (z4) in outer wing section. 20 m/s airspeed.

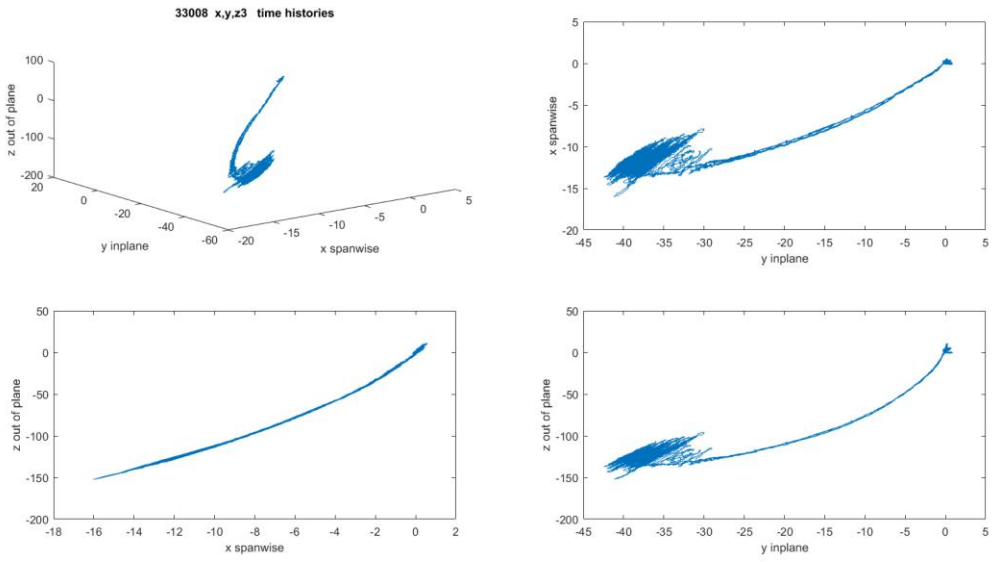

Figure 29. Deflections for wing-tip. 20 m/s and increasing root AOA.

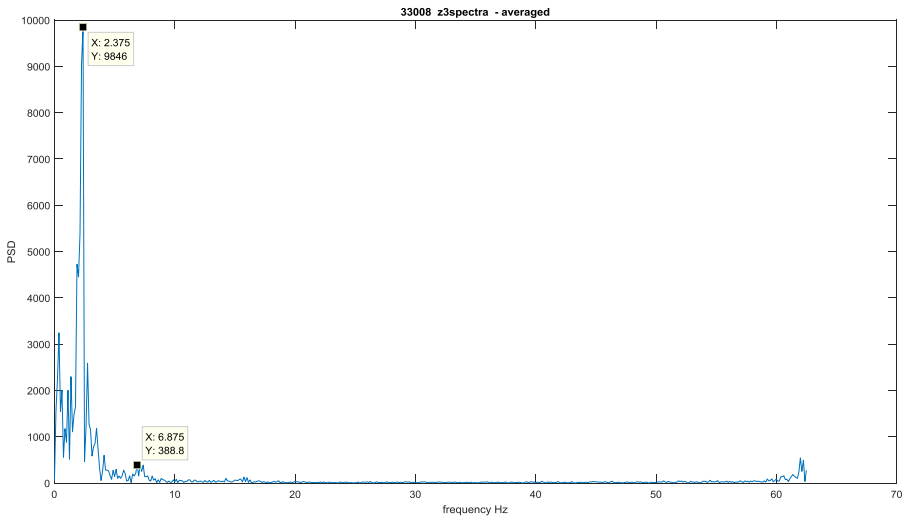

Figure 30. Averaged Spectra of LCO. 20 m/s.

6 CONCLUSIONS

The design and manufacture of a very flexible 2.4m semi-span high aspect ratio wing wind tunnel model is described. A series of low speed wind tunnel tests were performed to generate displacement, acceleration, strain gauge, aerodynamic pressure and six component balance measurements for a range of air-speeds and wing root angles of attack. Numerous static and dynamic measurements were made. Preliminary results were shown for the static and dynamic, structural and aerodynamic behaviour over a range of different airspeeds and root angle of attack. A very rich set of data has been generated. The wing demonstrated significant nonlinear static deflection behaviour and demonstrated geometric nonlinearities. From a dynamic viewpoint, several cases of LCOs were found due to geometric and separated flow effects. Further publications will consider each aspect (static, dynamic and limit cycle oscillations) of the tests in detail, including comparison with numerical models.

7 ACKNOWLEDGMENTS

This work was performed as part of the Innovate UK / Aerospace Technology Institute funded Agile Wing Integration (AWI) project. The authors are grateful for the assistance of the Airbus Filton Wind Tunnel Team in the running of these tests, Nick Hancock for his contribution to the wind tunnel model design and the Airbus Protospace team for the design and manufacture of the tip device.

8 REFERENCES

[1] Kroo, I., “DRAG DUE TO LIFT: Concepts for Prediction and Reduction,” *Annual Review of Fluid Mechanics*, Vol. 33, 2000, pp. 587–617.

[2] D. Calderon; J.E. Cooper; M.H. Lowenberg; S. Neild AIAA-2018-1680. On the Effect of Including Geometric Nonlinearity in the Sizing of a Wing SCITECH 2018

[3] Géradin, M., and Cardona, A., *Flexible Multibody Dynamics - A Finite Element Approach*, Wiley, Chichester, England, U.K., 2001.

[4] Hesse, H., Palacios, R., and Murua, J., “Consistent Structural Linearization in Flexible Aircraft Dynamics with Large Rigid-Body Motion,” *AIAA Journa*l v52 n3 (2014).

[5] Cesnik, C. E. S., and Brown, E. L., "Modeling of High Aspect Ratio Active Flexible Wings for Roll Control," *43rd AIAA/ASME/ASCE/AHS/ASC Structures, Structural Dynamics, and Materials Conference*, Denver, Colorado, 2002.
[6] Shearer, C. M., and Cesnik, C. E. S., "Nonlinear Flight Dynamics of Very Flexible Aircraft," *Journal of Aircraft*, Vol. 44, No. 5, 2007, pp. 1528–1545
[7] Su, W., and Cesnik, C. E. S., "Nonlinear Aeroelasticity of a Very Flexible Blended-Wing-Body Aircraft," *Journal of Aircraft*, Vol. 47, No. 5, 2010, pp. 1539–1553.
[8]C Howcroft, RG Cook, SA Neild, MH Lowenberg, JE Cooper, EB Coetzee. On the Geometrically Exact Low Order Modelling of a Flexible Beam: Formulation and Numerical Tests. *Proc Roy Soc A* 2018 v474 n 2216.
[9] Hodges, D. H., "A Mixed Variational Formulation Based on Exact Intrinsic Equations or Dynamics of Moving Beams,"
International Journal of Solids and Structures, Vol. 26, No. 11, 1990, pp. 1253–1273.
[10] Roger, K. L., "Airplane Math Modeling for Active Control Design," *Proceedings of the 44th AGARD Structure and Materials Panel*, 1977, pp. 4.1–4.11.
[11] Karpel, M., "Time Domain Aeroservoelastic Modeling Using Weighted Unsteady Aerodynamic Forces," *Journal of Guidance, Control and Dynamics*, Vol. 13, No. 1, 1990, pp. 30–37. doi:10.2514/3.20514.
[12] Harmin MY & Cooper JE, "Aeroelastic Behaviour of a Wing Including Geometric Nonlinearities" *Aeronautical Journal*. V115 n 1174. Dec 2011.pp 767 – 788.
[13] Patil, M. J., Hodges, D. H., and Cesnik, C. E. S., "Nonlinear Aeroelasticity and Flight Dynamics of High-Altitude Long-Endurance Aircraft," *Journal of Aircraft*, Vol. 38, No. 1, 2001, pp. 88–94.
[14] Cook, R. G., Palacios, R., and Goulart, P., "Robust Gust Alleviation and Stabilization of Very flexible Aircraft," *AIAA Journal*, Vol. 51, No. 2, 2013, pp. 330–340. doi:10.2514/1.J051697.
[15] Peters, D. A., Karunamoorthy, S., and Cao, W., "Finite State Induced Flow Models. Part 1: Two-Dimensional Thin Airfoil," *Journal of Aircraft*, Vol. 32, No. 2, 1995, pp. 313–322. doi:10.2514/3.46718.
[16] Leishman, J. G., "Unsteady Lift of a Flapped Airfoil by Indicial Concepts," *Journal of Aircraft*, Vol. 31, No. 2, 1994, pp. 288–297.
[17] Petot, D., "Differential Equation Modelling of Dynamic Stall," *La Reserche Aerospatiale*, No. 5, 1989, pp. 59–71.
[18] Leishman, J. G., and Beddoes, T. S., "A generalized Model for Airfoil Unsteady Aerodynamic Behaviour and Dynamic Stall Using the Indicial Method," *Proceedings of the 42nd Annual Forum of the American Helicopter Society*, Washington D. C., 1986, pp. 528–538.
[19] Kier, T. M., "Comparison of Unsteady Aerodynamic Modelling Methodologies with respect to Flight Loads Analysis," *AIAA Atmospheric Flight Mechanics Conference and Exhibit*, San Francisco, California, 2005.
[20] Palacios, R., Murua, J., and Cook, R. G., "Structural and Aerodynamic Models in the Nonlinear Flight Dynamics of Very Flexible Aircraft," *AIAA Journal*, Vol. 48, No. 11, 2010, pp. 2648–2659.
[21] Wang, Z., Chen, P. C., Liu, D. D., and Mook, D. T., "Nonlinear Aeroelastic Analysis for A HALE Wing Including Effects of Gust and Flow Separation," *48th AIAA/ASME/ASCE/AHS/ASC Structures, Structural Dynamics, and Materials Conference*, Honolulu, Hawaii, 2007.
[22] Murua, J., Hesse, H., Palacios, R., and Graham, J. M. R., "Stability and Open-Loop Dynamics of Very Flexible Aircraft

Including Free-Wake Effects," *52nd AIAA/ASME/ASCE/AHS/ASC Structures, Structural Dynamics and Materials Conference*, Denver, Colorado, 2011.
[23] Howcroft, H., Cook, R. G., Calderon, D. E., Lambert, L. A., Castellani, M., Cooper, J. E., Lowenberg, M. H., Nield, S. A., and Coetzee, E. B., "Aeroelastic Modelling of Highly Flexible Wings," *57th AIAA/ASCE/AHS/ASC Structures, Structural Dynamics, and Materials Conference*, San Diego, California, 2016.
[24] Deman Tang and Earl H. Dowell. Experimental and Theoretical Study on Aeroelastic Response of High-Aspect-Ratio Wings *AIAA Journal* Vol. 39, No. 8, August 2001
[25] Deman Tang and Earl H. Dowell. Limit-Cycle Hysteresis Response for a High-Aspect-Ratio Wing Model. *Journal of Aircraft* Vol. 39, No. 5, September–October 2002
[26] J-N Juang and R S Pappa, An Eigensystem Realization Algorithm for Modal Parameter Identification and Model Reduction. *Journal of Guidance, Control, and Dynamics*. 8 (5): 620–627. 1985.

COPYRIGHT STATEMENT